

Wireless-Enabled Asynchronous Federated Fourier Neural Network for Turbulence Prediction in Urban Air Mobility (UAM)

Tengchan Zeng, *Student Member, IEEE*, Omid Semiari, *Member, IEEE*,
Walid Saad, *Fellow, IEEE*, and Mehdi Bennis, *Fellow, IEEE*

Abstract

To meet the growing mobility needs in intra-city transportation, the concept of urban air mobility (UAM) has been proposed in which vertical takeoff and landing (VTOL) aircraft are used to provide a ride-hailing service. In UAM, aircraft can operate in designated air spaces known as *corridors*, that link the aerodromes, thus avoiding the use of complex routing strategies such as those of modern-day helicopters and alleviating the burden on the ground transportation system. For safety, a UAM aircraft must use air-to-ground communications to report flight plan, off-nominal events, and real-time movement to ground base stations (GBSs). A reliable communication network between GBSs and aircraft enables UAM to adequately utilize the airspace and create a fast, efficient, and safe transportation system. In this paper, to characterize the wireless connectivity performance for UAM, a suitable spatial model is proposed. For the considered setup, assuming that any given aircraft communicates with the closest GBS, the distribution of the distance between an arbitrarily selected GBS and its associated aircraft and the Laplace transform of the interference experienced by the GBS are derived. Using these results, the signal-to-interference ratio (SIR)-based connectivity probability is determined to capture the connectivity performance of the UAM aircraft-to-ground communication network. Then, leveraging these connectivity results, a wireless-enabled asynchronous federated learning (AFL) framework that uses a Fourier neural network is proposed to tackle the challenging problem of turbulence prediction during UAM operations. For this AFL scheme, a staleness-aware global aggregation scheme is introduced to expedite the convergence to the optimal turbulence prediction model used by UAM aircraft. Simulation results

A preliminary version was presented at the IEEE Global Communications Conference, 2021 [1]. This research was supported by the Office of Naval Research (ONR) under MURI Grant N00014-19-1-2621, the U.S. National Science Foundation under Grants CNS-1941348, and CNS-2008646, and by the Academy of Finland Project CARMA, by the Academy of Finland Project MISSION, by the Academy of Finland Project SMARTER, as well as by the INFOTECH Project NOOR.

T. Zeng and W. Saad are with Wireless@VT, Department of Electrical and Computer Engineering, Virginia Tech, Blacksburg, VA, 24061 USA. E-mail: {tengchan, walids}@vt.edu.

O. Semiari is with the Department of Electrical and Computer Engineering, University of Colorado, Colorado Springs, CO, 80918 USA. E-mail: osemiari@uccs.edu.

M. Bennis is with the Centre for Wireless Communications, University of Oulu, 90014 Oulu, Finland. E-mail: mehdi.bennis@oulu.fi.

validate the theoretical derivations for the UAM wireless connectivity. The results also demonstrate that the proposed AFL framework converges to the optimal turbulence prediction model faster than the synchronous federated learning baselines and a staleness-free AFL approach. Furthermore, the results characterize the performance of wireless connectivity and convergence of the aircraft's turbulence model under different parameter settings, offering useful UAM design guidelines.

I. INTRODUCTION

According to the world urbanization prospects released by the United Nations, by 2030, more than 60% of the world's population will live in urban areas and this percentage will jump to 70% by 2050 [2]. Given this growth, mobility demands will push the ground transportation system to its limits, leading to a long commute for the public and significant economic costs for the society. In order to meet future mobility needs, the novel concept of Urban air mobility (UAM) was proposed [3]. UAM will introduce vertical takeoff and landing (VTOL) aircraft to integrate the third dimension, i.e., airspace above cities, into the urban transportation system. Recent technology advances on distributed electric propulsion, electrical energy storage, lightweight airframe structures, and electric VTOL are rapidly making UAM a reality [3].

A. UAM System Overview

As shown in Fig. 1, a UAM system is composed of VTOL aircraft, aerodromes, corridors, and ground base stations (GBSs). In particular, aerodromes are designed to support the arrival and departure operation of the aircraft. Moreover, the corridors linking different aerodromes constitute the airspace designated for UAM operations. Different from complex routing strategies currently used for helicopter applications, the idea of corridors can dramatically reduce the complexity of operations [3]. Also, due to common mobility patterns shared by the public, corridors are usually concentrated around centralized points (CPs), such as residential, shopping, and business areas. In addition, GBSs in UAM will function as service providers that constantly communicate with the aircraft and deliver necessary information (e.g., weather and terrain), approve the flight plan submitted by the aircraft, and monitor the aircraft movements.

Each UAM operation has two major phases: *planning* and *en-route*. In the planning phase, once an aircraft receives a travel request between two aerodromes from an individual customer, it will determine the flight plan (e.g., the route selection of corridors, estimated travel time, and the aerodromes) which is subsequently submitted to a GBS via an air-to-ground link. Then, the GBS

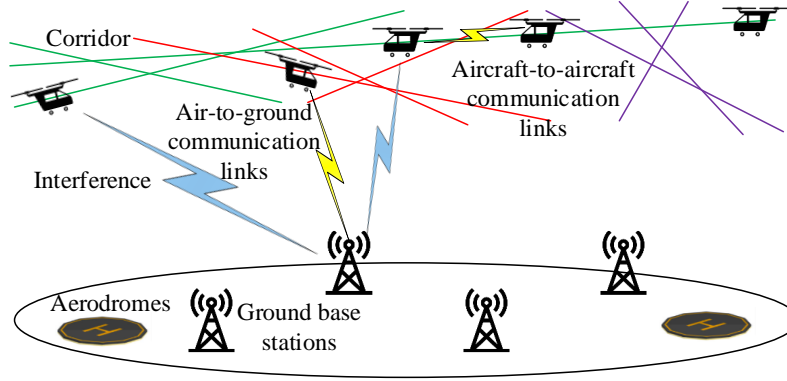


Fig. 1. Illustration of the UAM system which is composed of VTOL aircraft, aerodromes, corridors, and GBSs. To secure a safe operation, the UAM aircraft will constantly communicate with the GBS to submit the flight plan and convey off-nominal events.

will evaluate the submitted plan against pre-determined constraints, such as the availability of corridors and aerodromes as well as possible conflicts with on-going operation of other aircraft. If the flight plan meets these pre-determined constraints, then the GBS will approve the flight plan and share it with other GBSs via backhaul links. The aircraft will later operate in an en-route phase to pick up customers, navigate along the selected corridors, and arrive at the destination aerodrome within an anticipated travel time. Note that, during the en-route phase, the aircraft must constantly communicate with the GBSs to convey any off-nominal events (e.g., deviation from the selected corridors) due to high winds and navigation degradation, as well as to accordingly update its flight plan.

B. Motivation and Related Works

Since UAM operation is still at its infancy, most of the related research focus on market studies [4], public acceptance [5], and operational constraints [6]. There are few works studying the technical aspects of UAM operation. For example, a learning-based collision avoidance is proposed in [7] to allow multiple aircraft operating independently and keeping a safe distance among each other. In [8], the arrival process of aircraft is optimized to minimize the energy consumption while meeting the expected travel time. Moreover, the air traffic management is studied in [9] and [10] to navigate the UAM aircraft through obstacles in a congested urban area. In addition, the authors in [11] propose a battery model to quantify the effect of battery aging on the performance of electric flight in UAM. It is clear that, despite of the important role

of communication networks in UAM operation, there is a lack of a rigorous, holistic analysis of the wireless connectivity of aircraft-to-GBS communication network in UAM.

Beyond analyzing the connectivity needs of aircraft, another challenge in the UAM operation will be dealing with turbulence, i.e., air flow velocity changes around the aircraft [12]. Different from commercial jet aircraft, UAM aircraft are more likely to be affected by turbulence due to the following two facts. First, UAM aircraft can only operate at the troposphere [3] where the aerodynamics are constantly changing because of varying terrains, altitudes, and temperatures, in contrast to the commercial jets which usually cruise in the stable stratosphere. Second, compared to commercial jets, the lighter weight and smaller size of UAM aircraft will increase their susceptibility to turbulence, imposing a huge safety risk for passengers. However, if the air flow velocity can be predicted over time, UAM aircraft can take proper actions (i.e., yaw, pitch, and roll) to adjust their rotations and movements so as to minimize the impact of turbulence on the overall operation, avoiding the deviation from corridors and securing the safety. Hence, an accurate turbulence prediction will be a key enabler for the UAM operation.

To perform turbulence prediction, there is an increased interest in studying physical informed neural networks where the physical knowledge is integrated into the neural network design. For example, the authors in [13] and [14] use neural networks to build a mapping between the input data (e.g., temperature and pressure) and turbulence predictions in the Euclidean space. In contrast, the Fourier neural network (FNN), proposed in [15], considers data in the Fourier space. The motivation behind the use of FNN is that fluid dynamics (e.g., turbulence flow) are usually composed of components at different frequencies where the general direction is controlled by components at low frequency and the little eddies in the fluid flow are consisted of high-frequency components. By considering the input and output in the Fourier space, FNN can achieve a better accuracy than other learning based turbulence prediction models [15]. However, when using the learning methods proposed in [13]–[15] for turbulence prediction, the local data can be insufficient to train the learning model due to the limited on-chip memory available on board UAM aircraft. As a result, when the UAM aircraft operate in a new environment or encounters less frequently occurred events (e.g., poor weather), the turbulence models in [13]–[15] can fail to adapt to such changes, jeopardizing the operation safety. Therefore, an effective turbulence predictor design will directly depend on *collaboratively and jointly* training the prediction model among multiple UAM aircraft. To this end, one can use federated learning (FL) [16] to build a cooperative learning framework in which a centralized unit, such as the GBS, aggregates the

knowledge learned by a group of UAM aircraft.

However, it will be challenging to use conventional FL frameworks [17]–[25] for UAM aircraft turbulence prediction. On the one hand, synchronous FL algorithms, such as those in [17]–[21], are not suitable for UAM aircraft turbulence prediction due to the following two reasons. First, for synchronous FL frameworks, like FedAvg [17] and FedProx [18], UAM aircraft will suffer from the straggler effect where some local aircraft take much longer time than others to send their learned knowledge to the GBS, thereby increasing the convergence time and jeopardizing the aircraft’s ability to quickly predict the turbulence. Second, for synchronous FL schemes, like scalable FL [19], FedPAQ [20], and DFP [21], not all UAM aircraft can participate in the FL training and some important local model updates can be discarded, leading to a poor real-time turbulence prediction performance. On the other hand, since the staleness associated with the local trained model parameters is not properly considered, the prior work on asynchronous FL (AFL) [22]–[25] is not suitable for handling the UAM turbulence prediction task. For instance, these prior works either ignore staleness (e.g., [22] and [23]) or consider impractical assumptions, like bounded staleness [24] and [25], in their designed frameworks. However, because of the varying wireless channel conditions and mobility of aircraft, the staleness associated with the local model update will be unbounded and also vary from one UAM aircraft to another. If not being properly considered in the AFL framework design, such a unbounded and randomly distributed staleness can impede the convergence to the optimal turbulence prediction model used by UAM aircraft [26].

C. Contributions and Outcomes

The main contributions of this paper is a wireless-enabled AFL framework in which UAM aircraft use the communication network to collaboratively train a federated FNN and perform efficient turbulence prediction. In particular, to characterize how aircraft leverage wireless connectivity for AFL, we propose a stochastic geometry based spatial model for GBSs, corridors, and aircraft in UAM system. Moreover, we perform the wireless connectivity analysis for aircraft-to-GBS communication network in UAM. Based on the wireless connectivity study, we propose a wireless-enabled AFL framework in which UAM aircraft use the wireless network to collaboratively optimize the FNN-based turbulence prediction model. To mitigate the impact of staleness on convergence, we study a staleness-aware AFL framework and analyze the convergence. The novelty of this work lies in the following key contributions:

- We perform a novel, rigorous performance analysis of aircraft-to-GBS communication networks in UAM. In particular, by leveraging Poisson point process (PPP), Poisson cluster process (PCP), and Poisson line process (PLP) from stochastic geometry, we model the spatial distribution of GBSs, corridors, and aircraft in UAM. Assuming that any given aircraft will communicate with the closest GBS, we further derive the Laplace transform of the interference experienced by a GBS and the communication distance distribution between the GBS and its associated aircraft. Using these results, we obtain the signal-to-interference ratio (SIR)-based connectivity probability for the aircraft-to-GBS communication network in UAM.
- We propose a wireless-enabled collaborative learning framework consisting of FNN and AFL to optimize the turbulence prediction model for UAM aircraft. In particular, the local UAM aircraft will train an FNN model using their own data and, then, transmit the trained FNN parameters to the GBS via the UAM wireless network. Next, the GBS will aggregate the received parameters and generate a new global model in an asynchronous fashion. Based on the wireless connectivity study, we derive the staleness distribution of local FNN updates received at the GBS and the number of UAM aircraft that participate in AFL.
- To mitigate the impact of staleness on the overall convergence, we propose a staleness-aware global aggregation scheme for performing AFL. In particular, unlike conventional FL frameworks [17]–[25], the proposed staleness-aware global aggregation scheme explicitly considers the unbounded and randomly distributed staleness of locally trained FNN parameters. We then analyze the convergence rate of the proposed AFL framework and highlight the importance of considering the staleness in the global aggregation.

Simulation results validate our theoretical analysis for the wireless connectivity study. Moreover, the results show that our AFL framework can achieve a faster convergence than the conventional synchronous FL counterparts and AFL framework without considering the staleness of local FNN parameters. In addition, the results show the wireless connectivity and FNN model convergence for different UAM parameter settings, offering useful system design insight for deploying UAM. *To the best of our knowledge, this is the first work that analyzes the connectivity performance of a UAM communication network and develops a staleness-aware AFL framework to optimize the turbulence prediction model for UAM aircraft.*

The rest of the work is organized as follows. Section II presents the system model for UAM. Section III provides a theoretical analysis of the aircraft’s wireless connectivity. Section IV

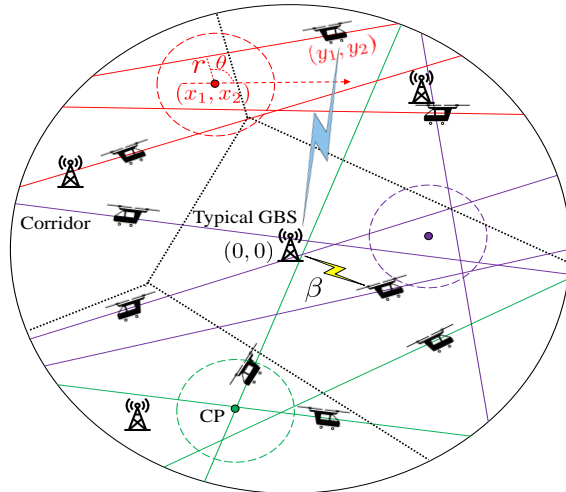


Fig. 2. The top view of how corridors, aircraft, centralized points, and GBSs are distributed in UAM.

introduces the staleness-aware AFL framework and analyzes the convergence. Section V provides simulation results, and conclusions are drawn in Section VI.

II. SYSTEM MODEL

Consider a group of UAM aircraft, as shown in Fig. 1. During flight, each aircraft will share a flight plan with other aircraft via aircraft-to-aircraft communications so as to maintain a safe distance and avoid collisions. Meanwhile, each aircraft constantly communicates with a GBS to report its location and possible off-nominal events, as well as transmit the turbulence prediction model updates.

A. Spatial Models for UAM

To characterize relative locations of different components in UAM, we must study the spatial modeling of aircraft and GBSs. As shown in Fig. 2, we model the distribution of GBSs as a two-dimensional PPP Ξ with density λ_b . For the distribution of aircraft, we first model the spatial distribution of CPs and corridors. In particular, to capture the fact that CPs can spread across space, we model their distribution as a two-dimensional PPP Φ with density λ_c . Around CP $i \in \Phi$, we model the distribution of corridors as a PLP Ψ_i with density λ_l where all corridors share the same height h . Since there will be a limited number of corridors around each CP, we assume that the maximum number of corridors for each CP is N . In this case, the number of corridors follows a truncated Poisson distribution within the range $[0, N]$.

Similar to [27], the relative location of a corridor around a CP is determined by two factors: the distance $r \in \mathbb{R}_+$ between the CP and the corridor and the angle $\theta \in [0, 2\pi)$ between the positive x -axis and the line perpendicular to the corridor, as shown in Fig. 2. However, instead of using a randomly distributed r in \mathbb{R}_+ that would not capture the realistic spatial location of centralized corridors, inspired by PCP [28], we model the distance r using the following two approaches. The first approach is aligned with the Thomas cluster process whereby we model the distance r as a truncated Gaussian distribution as follows: $f_R(r) = \sqrt{\frac{2}{\pi\sigma^2}} \exp\left(-\frac{r^2}{2\sigma^2}\right), r \in [0, \infty)$. In the second approach, we model the distance r as a uniform random variable within $[0, \hat{r}]$ with \hat{r} being the maximum distance from the CP, i.e., $f_R(r) = \frac{1}{\hat{r}}, r \in [0, \hat{r}]$. As such, we can guarantee that all corridors around the same CP will pass through a circular disc area with radius \hat{r} , similar to the definition of the Matern cluster process. With these two approaches, we can characterize the fact that the corridors are closely distributed around their CPs instead of being spread over the whole space as considered in [27]. Based on the real deployment and travel demands from the public, we can use either one of these two approaches to model the distance r . Next, on a randomly selected corridor $j \in \Psi_i$, we assume that the distribution of transmitting aircraft follows a one-dimensional PPP with density λ_t .

B. Aircraft-to-GBS Communication Model

Similar to prior works [29]–[31], we assume that each aircraft will be served by the closest GBS. Due to the stationarity of the two-dimensional PPP, we arbitrarily select a GBS as the *typical GBS* and assume that it is located at the origin with zero height. Thus, we can calculate the received signal power at the typical GBS from its associated aircraft as

$$P = pg(h^2 + \beta^2)^{-\frac{\alpha}{2}}, \quad (1)$$

where p is the transmit power used by all aircraft, and β is the distance between the vertical projection of the associated GBS at the plane with height h and the associated aircraft. α is the path loss exponent, and g is the air-to-ground wireless channel gain. We model the communication channels as independent Nakagami channels with an integer m to characterize a wide range of fading environment.

While receiving the transmission from the associated aircraft, the typical GBS will experience interference from two sources. The first one relates to aircraft who communicate with other GBSs rather than the typical GBS. The second interference source is aircraft who share the flight plan

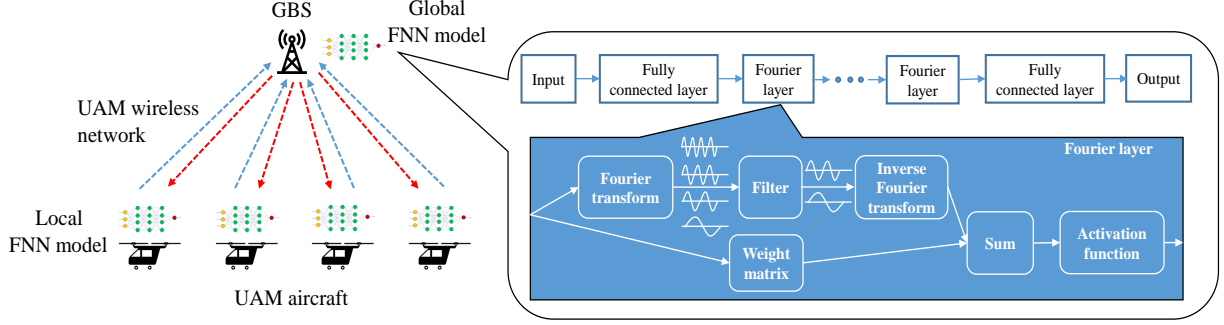


Fig. 3. UAM aircraft use a combination of FNN and AFL to optimize the turbulence prediction.

with surrounding aircraft. Taking into account the distribution of the transmitter aircraft in UAM, we can calculate the interference at the typical GBS as follows

$$I = \sum_{i \in \Phi} \sum_{j \in \Psi_i} \sum_{k \in \Omega_{i,j}} pg'(\|\mathbf{x} + \mathbf{y}\|^2 + h^2)^{-\frac{\alpha}{2}}, \quad (2)$$

where, as shown in Fig. 2, $\mathbf{x} = (x_1, x_2)$ is the location of CP $i \in \Phi$ relative to the vertical projection of the typical GBS at the plane of height h , and $\mathbf{y} = (y_1, y_2)$ denotes the relative location of an interfering aircraft compared to its CP.

C. Learning Model

To accurately predict turbulence, the UAM aircraft will use a combination of FNN and asynchronous FL. In particular, the aircraft will use the architecture of FNN [15] to train their local data, as shown in Fig. 3. The input and output for the FNN will be, respectively, the turbulence flow history data and prediction. Different from conventional machine learning methods that build an approximated function between the inputs and outputs defined in the Euclidean space, the FNN consists of Fourier layers whereby the data in the Fourier space is explicitly considered. The reason for considering data in the Fourier space is due to the fact that the turbulence flow can be decomposed into components at different frequencies. As shown in Fig. 3, by filtering out the components at high frequencies in the Fourier layers, the FNN can reduce the impact of high-frequency noise existing in the data collected at the aircraft, and, thereby, increase the turbulence prediction accuracy.

In AFL, the GBS will act as the parameter server and the set \mathcal{K} of K associated aircraft will collaboratively learn the FNN-based turbulence prediction model. In particular, the GBS will

first generate an initial global FNN parameters \mathbf{w}_0 for the FNN model and broadcast it to all associated aircraft. Then, the aircraft will use the received FNN parameters to train its local data and transmit the updated FNN parameters back to the associated GBS in the uplink. Next, whenever receiving the local FNN parameter updates from any arbitrary aircraft, the GBS will update the global FNN parameters and share the updated parameters with the corresponding aircraft. This AFL process is repeated over uplink-downlink channels between the GBS and the associated aircraft, and the global and local FNN parameters will be sequentially updated. As communication rounds proceed, the model will converge to the optimal turbulence prediction model which is the solution to the following optimization problem:

$$\arg \min_{\mathbf{w}} \sum_{k=1}^K \sum_{j=1}^{s_k} \frac{s_k}{s_K} f_k(\mathbf{w}, \xi_j), \quad (3)$$

$$\text{s.t. } \mathbf{w}^{(1)} = \mathbf{w}^{(2)} = \dots = \mathbf{w}^{(K)} = \mathbf{w}, \quad (4)$$

where $s_K = \sum_{k=1}^K s_k$ is the size of the training data across all aircraft with s_k being the size of training data at aircraft k . $f_k(\mathbf{w}, \xi_j)$ is the loss function of aircraft $k \in \mathcal{K}$ when using the FNN model parameter \mathbf{w} to train local data ξ_j , and $f_k(\mathbf{w}) = \sum_{j=1}^{s_k} f_k(\mathbf{w}, \xi_j)$ is the total loss at aircraft $k \in \mathcal{K}$.

Clearly, in the local FNN training phase, some aircraft use the most updated global model while others can only train stale versions of global model over their data. Given the higher computing power and larger communication bandwidth of a GBS, the local FNN parameters can be updated immediately once the GBS receives the trained model updates from the corresponding aircraft. In this case, *the staleness associated to local FNN parameters can thereby defined as the time elapsed since the generation of the local model parameter update that is most recently received at the GBS*. If the aircraft complete the local model training and model parameter transmission with less time, their trained FNN parameters will be associated with less staleness. Hence, staleness can be calculated as the time spent on the FNN model training and FNN parameters transmission. For the FNN model training, the computing delay can be derived as $t_{\text{comp}} = \frac{v\epsilon}{\varepsilon}$, where v is size of training data, ϵ refers to the number of computing cycles needed per bit, and ε is the frequency of CPU clock of UAM aircraft. When calculating the transmission delay, for tractability, we assume that the noise is negligible compared to the interference. Therefore, given the received signal and interference calculated in (1) and (2), the transmission delay will be as $t_{\text{tran}} = \frac{V}{W \log_2(1 + \frac{P}{I})}$, where V is the size of the data packet containing the FNN parameters and

W is the communication bandwidth. Hence, the staleness associated to the locally trained FNN parameters will be given by $\delta = t_{\text{comp}} + t_{\text{tran}}$.

When designing the AFL framework to optimize the turbulence prediction model for UAM aircraft, we need to address a number of challenges. First, to characterize the convergence of the AFL framework, we must determine the number of UAM aircraft that participate in AFL and the staleness distribution of local FNN updates. To this end, one can use tools from stochastic geometry to analyze the performance of a UAM communication network. However, existing stochastic geometry approaches, such as those in [29]–[31], cannot be directly applied to our model. This is because, different from conventional networks (e.g., cellular systems) that can be simply modeled by a single point process, the spatial distribution of UAM aircraft is characterized by a combination of PPP, PCP, and PLP. Meanwhile, due to the fading channels in the UAM wireless network and the mobility of UAM aircraft, the staleness of locally trained FNN parameters will be unbounded and randomly distributed. If the AFL framework is not designed properly, such varying staleness can have a detrimental effect on the overall convergence. Hence, the second challenge will be determining and mitigating the impact of such unbounded and randomly distributed staleness on the overall FNN model convergence. In this way, UAM aircraft can quickly and accurately make the turbulence prediction and take proper actions to secure the operation safety.

In Section III, we take into account the complex distribution of UAM aircraft and analyze the connectivity performance as well as derive the staleness distribution of local FNN parameters and the number of aircraft participating in the AFL. Then, we propose a staleness-aware AFL framework and analyze its convergence in Section IV.

III. PERFORMANCE ANALYSIS OF UAM AIRCRAFT-TO-GBS COMMUNICATION NETWORK

First, we characterize the distance distribution of the typical GBS and its associated aircraft. Then, we calculate the Laplace transform of the interference experienced by the typical GBS. Next, we derive the SIR-based connectivity probability for the aircraft when operating in the UAM corridors. Based on these results, we derive the distribution of staleness of local FNN parameters and the number of aircraft that participate in the AFL.



Fig. 4. Four possible relative locations between CP and corridors where the black solid point, red solid point, and solid line, respectively, show the aircraft, CP, and corridor.

A. Distance Distribution between the Typical GBS and its Associated Aircraft

Since each aircraft communicates with its closest GBS, we can derive the statistical distribution of the distance β between the vertical projection of the typical GBS and its associated aircraft in the following lemma that follows from [31].

Lemma 1. For a group of GBSs whose distribution follows a two-dimensional PPP with density λ_b , the probability density function (PDF) of the distance β between the vertical projection of the typical GBS and its associated aircraft is $f_B(\beta) = 2\pi\lambda_b\beta \exp(-\lambda_b\pi\beta^2)$.

With Lemma 1, we can find the statistical distribution of the distance between the typical GBS and its associated aircraft at height h and further use (1) to determine the received signal power at the typical GBS.

B. Laplace Transform of Interference at the Typical GBS

In order to capture the interference experienced by the typical GBS, we need to model the distance between the typical GBS and the interfering aircraft. To this end, we start with the relative location $\mathbf{y} = (y_1, y_2)$ of the interfering aircraft around its CP. As shown in Fig. 4, we list four possible relative locations between CP and corridors. Assume that the projected point of CP on the corridor is $\mathbf{z} = (z_1, z_2)$ and the distance between \mathbf{z} and the aircraft is $u \in \mathbb{R}$. Hence, we can obtain the four alternatives for the location of aircraft on the corridor as

$$\begin{cases} (z_1 + u \cos(\frac{\pi}{2} - \theta), z_2 - u \sin(\frac{\pi}{2} - \theta)), & \text{if } \theta \in [0, \frac{\pi}{2}), \\ (z_1 + u \cos(\theta - \frac{\pi}{2}), z_2 + u \sin(\theta - \frac{\pi}{2})), & \text{if } \theta \in [\frac{\pi}{2}, \pi), \\ (z_1 - u \cos(\frac{3\pi}{2} - \theta), z_2 + u \sin(\frac{3\pi}{2} - \theta)), & \text{if } \theta \in [\pi, \frac{3\pi}{2}), \\ (z_1 - u \cos(\theta - \frac{3\pi}{2}), z_2 - u \sin(\theta - \frac{3\pi}{2})), & \text{if } \theta \in [\frac{3\pi}{2}, 2\pi). \end{cases}$$

Meanwhile, the location of the CP can be given by:

$$\begin{cases} (z_1 - r \cos(\theta), z_2 - r \sin(\theta)), & \text{if } \theta \in [0, \frac{\pi}{2}), \\ (z_1 + r \sin(\theta - \frac{\pi}{2}), z_2 - r \cos(\theta - \frac{\pi}{2})), & \text{if } \theta \in [\frac{\pi}{2}, \pi), \\ (z_1 + r \sin(\frac{3\pi}{2} - \theta), z_2 + r \cos(\frac{3\pi}{2} - \theta)), & \text{if } \theta \in [\pi, \frac{3\pi}{2}), \\ (z_1 - r \cos(2\pi - \theta), z_2 + r \sin(2\pi - \theta)), & \text{if } \theta \in [\frac{3\pi}{2}, 2\pi). \end{cases}$$

Given the locations of the aircraft and CP for $\theta \in [0, 2\pi)$, we have $\mathbf{y} = (u \sin \theta + r \cos \theta, -u \cos \theta + r \sin \theta)$, $r \in \mathbb{R}_+$ and $u \in \mathbb{R}$. Therefore, the distance between the vertical projection point of the typical GBS and the interfering aircraft is $f(x_1, x_2, u, r, \theta) = \|\mathbf{x} + \mathbf{y}\| = (x_1 + u \sin \theta + r \cos \theta)^2 + (x_2 - u \cos \theta + r \sin \theta)^2)^{1/2}$. Hence, we can determine the Laplace transform of the interference experienced by the typical GBS in the following lemma.

Lemma 2. When UAM aircraft operating within the corridors are distributed according to the one-dimensional PPP, the Laplace transform of the interference experienced by the typical GBS is

$$\mathcal{L}(s) = \exp \left(-\lambda_c \int_{\mathbb{R}^+} \int_0^{2\pi} \left(1 - \sum_{n=0}^N (\mathcal{K}_2(l \cos \phi, l \sin \phi))^n \mathbb{P}(n|n < N) \right) l d\phi dl \right), \quad (5)$$

where $\mathbb{P}(n|n \leq N) = \frac{(\lambda_l - 1)^n e^{-(\lambda_l - 1)}}{n! \omega}$ with $\omega = \sum_{n=0}^N \frac{(\lambda_l - 1)^n e^{-(\lambda_l - 1)}}{n!}$, and $\mathcal{K}_2(l \cos \phi, l \sin \phi) = \int_{\mathbb{R}^+} \int_0^{2\pi} \mathcal{K}_1(l \cos \phi, l \sin \phi, r, \theta) f_R(r) f_\theta(\theta) d\theta dr$, with

$$\mathcal{K}_1(l \cos \phi, l \sin \phi, r, \theta) = \exp \left(-\lambda_t \int_{\mathbb{R}} 1 - \left(\left(1 + \frac{s(f^2(l \cos \phi, l \sin \phi, u, r, \theta) + h^2)^{-\frac{\alpha}{2}}}{m} \right)^{-m} \right) dt \right). \quad (6)$$

Proof: See Appendix A. ■

By choosing the proper function $f_R(r)$ in Lemma 2, we can calculate the Laplace transform of the interference when the distance between the corridor and its CP follows a truncated Gaussian distribution or a uniform distribution. Next, we use the Laplace transform of the interference obtained in Lemma 2 to determine the connectivity performance of UAM air-to-ground communications and the staleness distribution of locally trained FNN parameters.

C. Connectivity Probability and Staleness Distribution

The connectivity probability is defined as the probability with which the SIR received by the typical GBS exceeds a target threshold γ required for a successful communication. Based on the Laplace transform of the interference obtained in Lemma 2, we can derive the mathematical expression for the connectivity probability in the following theorem.

Theorem 1. When an arbitrarily selected aircraft communicates with its associated GBS in UAM, the connectivity probability can be calculated as

$$\mathbb{P}_{\text{conn}} = \int_{\mathbb{R}^+} \sum_{\hat{m}=1}^m (-1)^{\hat{m}+1} \binom{m}{\hat{m}} \mathcal{L}(\gamma \hat{m} \eta (h^2 + \beta^2)^{\frac{\alpha}{2}}) f_B(\beta) d\beta, \quad (7)$$

where $\eta = m(m!)^{-1/m}$.

Proof: See Appendix B. ■

From Theorem 1, we can theoretically analyze the connectivity performance of aircraft-to-GBS communication networks in UAM. The results in Theorem 1 also pave the way for optimizing the UAM design to achieve a reliable wireless connectivity and ensure an efficient and safe UAM operation. Based on the Theorem 1, we can derive the mathematical distribution of staleness associated to the FNN parameters, as shown in the following corollary.

Corollary 1. When an arbitrarily selected UAM aircraft participates in the AFL, the staleness of FNN parameters received at the GBS will follow a cumulative distribution function (CDF) as follows:

$$\mathbb{P}_{\text{staleness}}(\delta \leq \tau) = \int_{\mathbb{R}^+} \sum_{\hat{m}=1}^m (-1)^{\hat{m}+1} \binom{m}{\hat{m}} \mathcal{L} \left(\hat{m} \eta \left(2^{\frac{V}{W(\tau-t_{\text{comp}})}} - 1 \right) (h^2 + \beta^2)^{\frac{\alpha}{2}} \right) f_B(\beta) d\beta. \quad (8)$$

Proof: We replace γ in Theorem 1 with $2^{\frac{V}{W(\tau-t_{\text{comp}})}} - 1$ and the remaining proof is similar to Theorem 1. ■

From Corollary 1, we can observe how different UAM parameters, such as the densities of corridors, aircraft, CPs, and GBSs, and wireless parameters, like the Nakagami fading parameter, affect the staleness distribution of the local FNN model updates received at the GBS. To determine the convergence performance of AFL, we still need to derive the number of UAM aircraft that collaboratively learn the FNN-based turbulence prediction model.

D. Expected Number of Aircraft Participating in AFL

To determine the expected number of UAM aircraft participating in AFL, we consider a circular area with a radius R and, in the following lemma, we derive the intermediate results, i.e., the expected length of corridor existing in the circular area.

Lemma 3. For a circular area with radius R , the expected length of an arbitrarily selected corridor in UAM is

$$\mathbb{E}(L) = \int_{\mathbb{R}^+} \int_0^{2\pi} 2\sqrt{R^2 - (x_1 \cos \theta + x_2 \sin \theta + r)^2} f_R(r) f_\theta(\theta) d\theta dr. \quad (9)$$

Proof: See Appendix C. ■

Given the expected length of corridor calculated in Lemma 3, we can determine the density of PPP distributed aircraft on each corridor and further obtain the expected number of aircraft associated to the GBS and participating in the AFL in the following theorem.

Theorem 2. When UAM aircraft operate in a circular area with radius R , the expected number K of aircraft participating in the AFL framework will be given by:

$$K = \left\lfloor \frac{\lambda_c \lambda_t \mathbb{E}(L) \sum_{n=0}^N n \mathbb{P}(n|n < N)}{\lambda_b} \right\rfloor, \quad (10)$$

where $\lfloor \cdot \rfloor$ is the floor function.

Proof: See Appendix D. ■

From Theorem 2, we can determine the number of aircraft participating in AFL to collaboratively learn the turbulence prediction model. Next, based on the results in Corollary 1 and Theorem 2, we propose a staleness-aware AFL framework for UAM aircraft turbulence prediction and study its convergence.

IV. STALENESS-AWARE AFL FOR UAM AIRCRAFT TURBULENCE PREDICTION OPTIMIZATION

To mitigate the impact of stale local FNN parameters on the overall convergence, we consider a staleness-aware global aggregation scheme for AFL where the GBS will aggregate the local trained parameters and update the global FNN model as follows

$$\mathbf{w}_{i+1} = \mathbf{w}_i - \eta_i g_1(\delta_{k,i}) \frac{s_k}{s_K} \nabla f_k(\mathbf{w}_{\delta_{k,i}}). \quad (11)$$

In (11), η_i is the learning rate at communication round i , and $\delta_{k,i}$ captures the staleness of FNN parameters received at the GBS from aircraft $k \in \mathcal{K}$ at communication round i . $g_1(\delta_{k,i})$ is a monotonically decreasing function of the staleness $\delta_{k,i}$ so as to minimize the impact of stale FNN parameters on the learning performance. It is clear that the convergence of the turbulence prediction model depends on the expression of the monotonically decreasing function $g_1(\cdot)$ and the number of UAM aircraft participating in AFL. In the following subsection, we will determine the convergence conditions and analyze the convergence rate of AFL framework with the staleness-aware global aggregation scheme in (11).

A. Convergence Study of the Proposed AFL

Unlike the convergence study done in [24] where the staleness of local model updates is bounded, we will explicitly consider the randomly distributed and unbounded staleness derived in Corollary 1 and its impact on the overall AFL convergence. To this end, we make the following assumptions:

- The gradient function $\nabla f(\cdot)$ is uniformly Lipschitz continuous, i.e., for some positive parameter L , $\|\nabla f(\mathbf{w}_i) - \nabla f(\mathbf{w}_j)\| \leq L\|\mathbf{w}_i - \mathbf{w}_j\|$.
- The variance of the local gradient descent at an arbitrarily selected aircraft $k \in \mathcal{K}$ with respect to the counterpart for the whole training data across all aircraft is upper bounded, i.e., $\mathbb{E}\|\nabla f(\mathbf{w}) - \nabla f_k(\mathbf{w})\|^2 \leq \phi^2, \forall \mathbf{w} \in \mathbb{R}^d$, where ϕ^2 is the upper bound.
- The variance of the global gradient descent at communication round i with respect to the local gradient descent of the stale local FNN parameters $\mathbf{w}_{\delta_{k,i}}$ at aircraft k is upper bounded by a staleness-dependent value, i.e., $\mathbb{E}\|\nabla f(\mathbf{w}_i) - \nabla f(\mathbf{w}_{\delta_{k,i}})\|^2 \leq g_2(\delta_{k,i})\mathbb{E}\|\nabla f(\mathbf{w}_{\delta_{k,i}})\|^2$, where $g_2(\delta_{k,i})$ is a monotonically increasing function in terms of staleness $\delta_{k,i}$ with $g_2(0) = 0$ and $g_2(\infty) = 1$.

The first two assumptions are commonly used in the current literature, like [32]. In particular, the first assumption can be easily satisfied by some popular loss functions used for the turbulence prediction, such as the mean squared error [13]–[15]. The second assumption can be justified by the fact that the turbulence variations are bounded in real scenarios. For the third assumption, it originates from the basic convergence pattern in which the expected loss decreases as the number of communication rounds between the GBS and UAM aircraft increases. Using these three assumptions, we can derive the convergence rate of the proposed AFL to determine the expected loss reduced between two consecutive communication rounds in the following theorem.

Theorem 3. When the staleness-aware AFL framework is used to improve the turbulence prediction model for UAM aircraft, the convergence rate can be given by:

$$\mathbb{E}(f(\mathbf{w}_{i+1})) \leq f(\mathbf{w}_i) - \frac{\eta_i \mathbb{E}_\delta(g_1(\delta))}{2K} \|\nabla f(\mathbf{w}_i)\|^2 + \frac{L\eta_i^2 (\mathbb{V}_\delta(g_1(\delta)) + \mathbb{E}_\delta^2(g_1(\delta))) \phi^2}{2K^2}, \quad (12)$$

as long as the following condition is satisfied:

$$L\eta_i g_2(\delta_{k,i}) + L\eta_i g_1(\delta_{k,i}) - K \leq 0, \forall \delta_{k,i} \in \mathbb{R}_+, \quad (13)$$

where the mean is $\mathbb{E}_\delta(g_1(\delta)) = \int_0^\infty g_1(\tau) f_\delta(\tau) d\tau$ and the variance is $\mathbb{V}_\delta(g_1(\delta)) = \int_0^\infty g_1^2(\tau) f_\delta(\tau) d\tau - \mathbb{E}_\delta^2(g_1(\delta))$ with $f_\delta(\cdot)$ derived in Corollary 1.

Proof: See Appendix E. ■

Using Theorem 3, we can determine the convergence rate and convergence conditions when we use the proposed, staleness-aware AFL scheme to optimize the UAM aircraft turbulence prediction model. In particular, the convergence rate depends on the statistical properties (i.e., mean and variance) of randomly distributed staleness linked to local FNN parameters. Also, there are two convergence conditions: there must be at least $K = \lceil L\eta_i g_2(\delta_{k,i}) + L\eta_i g_1(\delta_{k,i}) \rceil$ UAM aircraft associated with the typical GBS; the monotonically decreasing function $g_1(\delta)$ must be chosen in a way that $K\mathbb{E}_\delta(g_1(\delta))\|\nabla f(\mathbf{w}_i)\|^2 \geq L\eta_i (\mathbb{V}_\delta(g_1(\delta)) + \mathbb{E}_\delta^2(g_1(\delta))) \phi^2$. In the following corollary, we also calculate the convergence rate when using the conventional aggregation, i.e., $\mathbf{w}_{i+1} = \mathbf{w}_i - \eta_i \frac{s_k}{s_K} \nabla f_k(\mathbf{w}_{\delta_{k,i}})$, so as to showcase the benefits of the staleness-aware global aggregation scheme in AFL.

Corollary 2. If the GBS does not consider the staleness associated to the received local FNN parameters in the global aggregation process, then, the convergence rate for AFL will be

$$\mathbb{E}(f(\mathbf{w}_{i+1})) \leq f(\mathbf{w}_i) - \frac{\eta_i}{2K} \|\nabla f(\mathbf{w}_i)\|^2 + \frac{L\eta_i^2 \phi^2}{2K^2}. \quad (14)$$

Proof: We can replace $g_1(\delta) = 1$ in Theorem 3 to obtain the convergence rate. ■

When $(\mathbb{E}_\delta(g_1(\delta)) - 1)\|\nabla f(\mathbf{w}_i)\| \geq \frac{L\eta_i \phi^2}{K} (\mathbb{V}_\delta(g_1(\delta)) + \mathbb{E}_\delta^2(g_1(\delta)))$, AFL with the staleness-aware global aggregation can achieve a faster convergence rate than the conventional AFL by comparing the results in Theorem 3 and Corollary 2. Based on Theorem 3, we further determine how fast the model converges to the optimal model in (3) when using the proposed AFL framework in the following corollary.

Table. I. Simulation parameters.

Parameters	Values
Height h	500 feet (152.4 m) [3]
CP density λ_c	$0.001 \text{ (km}^2\text{)}^{-1}$
GBS density λ_b	$1 \text{ (km}^2\text{)}^{-1}$
Corridor density λ_t	5 corridor/km ²
Aircraft density λ_t	1 aircraft/km
Maximum number of corridors N	10
Transmit power T_r	40 dBm
SIR threshold γ	0 dB
Bandwidth W	10 Mhz
Model parameter size V	5 kb
Path loss exponent α	4
Nakagami fading parameter m	1
Variance of truncated Gaussian distribution σ^2	1
Distance limitation for the uniform distribution \hat{r}	2 km
Training data size v	10^3 bits
Number of computing cycles needed per bit ϵ	10^3
Frequency of CPU clock ε	10^9 cycles/s

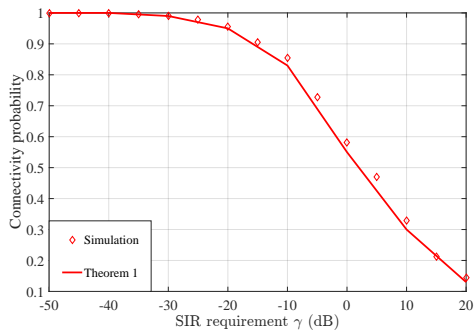
Corollary 3. If the loss function is differentiable and strongly convex with positive parameter c and the learning rate is fixed, i.e., $\eta_i = \eta$, the results in Theorem 3 can be simplified to

$$\mathbb{E}(f(\mathbf{w}_{i+1})) - f(\mathbf{w}^*) \leq \left(1 - \frac{\eta \mathbb{E}_\delta(g_1(\delta))c}{K}\right)^{i+1} (f(\mathbf{w}_0) - f(\mathbf{w}^*)) + \frac{L\eta(\mathbb{V}_\delta(g_1(\delta)) + \mathbb{E}_\delta^2(g_1(\delta)))\phi^2}{2K\mathbb{E}_\delta(g_1(\delta))c} \left(1 - \left(1 - \frac{\eta \mathbb{E}_\delta(g_1(\delta))c}{K}\right)^i\right), \quad (15)$$

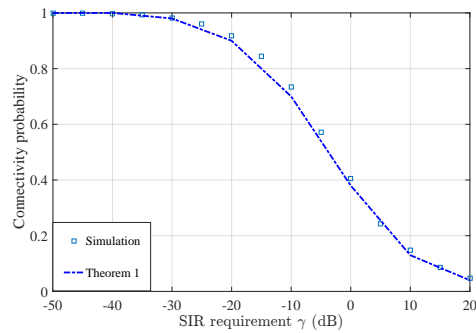
where \mathbf{w}^* is the solution to the optimization problem in (3).

Proof: See Appendix F. ■

The result in Corollary 3 shows that, as communication round i increases, there will be a gap, $\frac{L\eta(\mathbb{V}_\delta(g_1(\delta)) + \mathbb{E}_\delta^2(g_1(\delta)))\phi^2}{2K\mathbb{E}_\delta(g_1(\delta))c}$, between $\mathbb{E}(f(\mathbf{w}_{i+1}))$ and $f(\mathbf{w}^*)$. Clearly, this gap depends on the distribution of staleness associated to the local FNN parameters and the number of UAM aircraft participating in AFL. For instance, a larger K will lead to a smaller gap between $\mathbb{E}(f(\mathbf{w}_{i+1}))$ and $f(\mathbf{w}^*)$. Hence, to minimize the gap derived in Corollary 3 and improve the convergence performance, we can optimize the UAM parameter setting (e.g., select a proper density of corridors) and the wireless network design (e.g., transmit power).



(a) Truncated Gaussian distribution for the distance r between the CP and corridors.



(b) Uniform distribution for the distance r between the CP and corridors.

Fig. 5. Connectivity probability of the UAM wireless network versus the SIR threshold.

V. SIMULATION RESULTS

For our simulations, we model the UAM system as a circular area with a radius of 20 km. Simulation parameters are summarized in Table I. We first validate the theoretical analysis in Theorem 1 for the two discussed cases where the distance r follows a truncated Gaussian distribution and a uniform distribution. Then, we study how the densities of GBSs, CPs, corridors, and aircraft affect the wireless connectivity performance and provide insights into the system design guidelines for UAM. Next, we analyze the convergence of staleness-aware AFL framework in comparison to multiple baselines and highlight the merits of considering staleness in the AFL framework.

A. Validation of Theoretical Analysis

Fig. 5 shows the connectivity probability of the air-to-ground communication network versus the SIR threshold γ when the distance r follows a truncated Gaussian distribution and a uniform distribution. As observed from Fig. 5, the simulation results for both distributions match the analytical results with a small deviation. The small deviation stems from the use of the approximated tail probability of the Gamma function in Theorem 1. Fig. 5 also shows that, when the SIR threshold γ increases, the connectivity performance of the UAM's wireless network will degrade. This is because, with a higher target SIR threshold, fewer air-to-ground communication links will meet the connectivity requirement for a successful transmission.

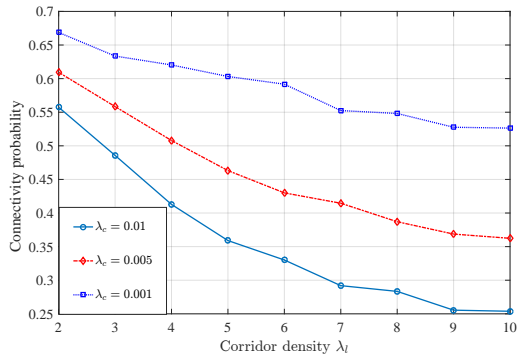


Fig. 6. Connectivity probability versus the corridor density under different cluster densities.

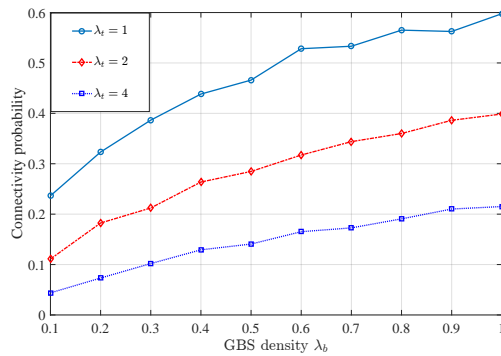


Fig. 7. Connectivity probability versus the GBS density under different aircraft densities.

B. Connectivity Performance of UAM under Different Parameter Settings

Fig. 6 shows the connectivity probability of the UAM wireless network versus the corridor density λ_l under different values for the cluster density λ_c when the distance follows a truncated Gaussian distribution. From Fig. 6, we observe that the connectivity probability decreases when λ_l increases. This is due to the fact that, with more corridors distributed around the CPs, the number of interfering aircraft will also increase, leading to a higher interference at the typical GBS and a degradation of the wireless connectivity performance. Moreover, Fig. 6 shows that a higher density of CPs will also degrade the UAM wireless connectivity performance. This is because a higher density of CPs will lead to more corridors and more interfering aircraft.

Fig. 7 shows the connectivity probability of the UAM wireless network versus the GBS density λ_b under different aircraft density λ_t on each corridor and for the case when the distance follows a truncated Gaussian distribution. As shown in Fig. 7, the connectivity probability increases when the GBS density λ_b increases. This is because, with more GBSs, the communication distance between a given GBS and its associated UAM aircraft will be reduced, leading to a higher received signal power and SIR. Moreover, Fig. 7 shows that the presence of more aircraft on corridors will negatively impact the connectivity probability performance. This can be explained that a higher λ_t will lead to a larger number of interfering aircraft. Note that the simulation results of the uniformly distributed distance r are similar to the counterparts when the distance follows a truncated Gaussian distribution, and they are omitted due to space limitations.

Based on the simulation results in Figs. 6 and 7, when the densities of aircraft, corridors, and CPs increase, the UAM wireless connectivity performance will degrade. To avoid this perfor-

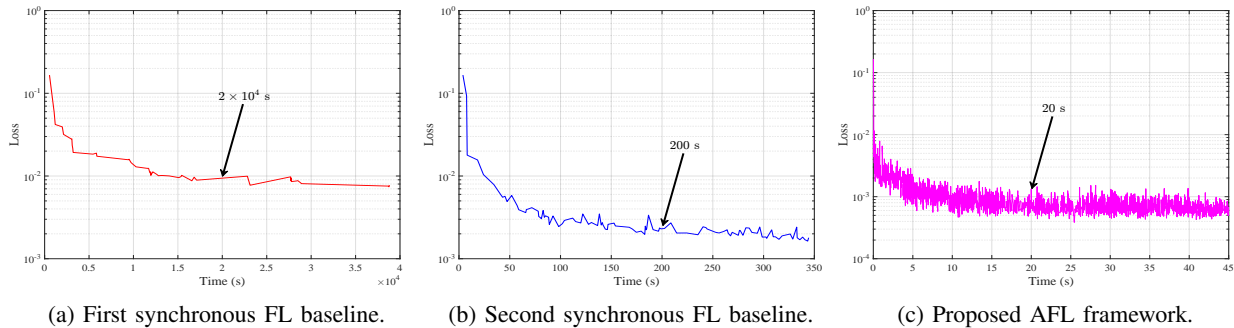


Fig. 8. Training performance of two synchronous FL baselines and our proposed AFL framework.

mance degradation, one can deploy more GBSs at the expense of site acquisition constraints and costs, particularly in urban environments. Therefore, realizing efficient UAM systems depends on a careful selection of design parameters to improve the wireless connectivity performance while reducing the overall deployment cost.

C. Convergence of AFL for Turbulence Prediction

In our simulation, when building the AFL framework, we generate the local training turbulence data for UAM aircraft by first randomly generating the velocity field $v_0(s)$ and, then, following the Burgers' equation [33] and [34]:

$$\frac{\partial v(s, t)}{\partial t} + \frac{1}{2} \frac{\partial v^2(s, t)}{\partial s} = \rho \frac{\partial v^2(s, t)}{\partial s \partial s}, v(s, 0) = v_0(s), \quad (16)$$

where $v(s, t)$ is the velocity of the turbulence flow at the location s and time t , and ρ is the kinematic viscosity coefficient. Note that, here, we use Burgers' equation as an example to generate the local training data, our proposed AFL framework can be used to deal with the training data generated by other partial differential equations (PDEs), like Navier-Stokes equation. In terms of the turbulence prediction model, we consider an FNN model with two Fourier layers. We randomly select a GBS and its associated aircraft to collaboratively learn the FNN model within the proposed AFL framework.

Fig. 8 shows the convergence of synchronous FL baselines and our proposed AFL framework. In particular, we select two popular synchronous FL baselines. In the first baseline, i.e., FedAvg [17], the GBS will generate a new global FNN model when all local aircraft finish the local model training and the model parameter transmission. In the second baseline, i.e., scalable FL [19], a new global FNN model will be generated at the GBS once it receives the locally

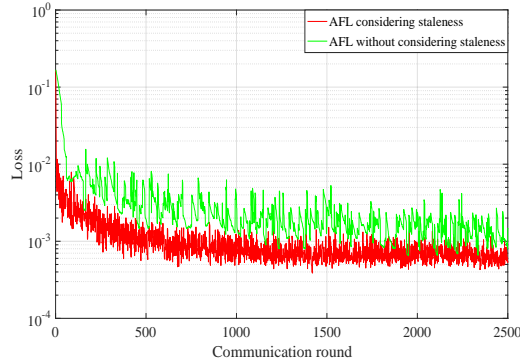


Fig. 9. Comparison between two AFL schemes with and without considering staleness.

trained parameters from half of its associated aircraft. As shown from Fig. 8, our proposed AFL framework can achieve a faster convergence compared to two synchronous counterparts. In particular, our proposed AFL framework can converge within 20 s, whereas the first and second baselines need to spend, 2×10^4 s and 200 s, to achieve convergence. In other words, our proposed AFL framework can improve the convergence rate by 99.9% and 90% compared to these two baselines. The reason is that, compared with the first baseline, our proposed framework will not suffer from the straggler effect where the aircraft who finish the local training and transmission fast have to wait for the slower ones. Also, our proposed AFL framework guarantees that the local model update from any aircraft will be considered in the global aggregation in contrast to the second baseline where some important local model updates can be discarded due to the long communication time.

In Fig. 9, we compare our proposed staleness-aware AFL framework with an AFL framework that aggregates the local model updates without considering staleness. In particular, for the AFL framework, we choose $g_1(\delta) = 1 + \exp(-\delta)$ in (11) based on the results derived in Corollary 2. In the AFL framework without considering the staleness, $g_1(\delta) = 1$. As observed from Fig. 9, the AFL framework considering the impact of staleness converges faster than the framework without considering the staleness of local model updates. In particular, to achieve a loss of 10^{-3} , our proposed AFL framework needs around 500 communication rounds, whereas the AFL framework without considering the staleness of local updates needs more than 2000 communication rounds. The reason is that, during the global aggregation in (11), the local model update can be generated by using the stale version of global model instead of the freshly generated one at UAM aircraft. Hence, directly aggregating such outdated local FNN parameters will inevitably slow down the

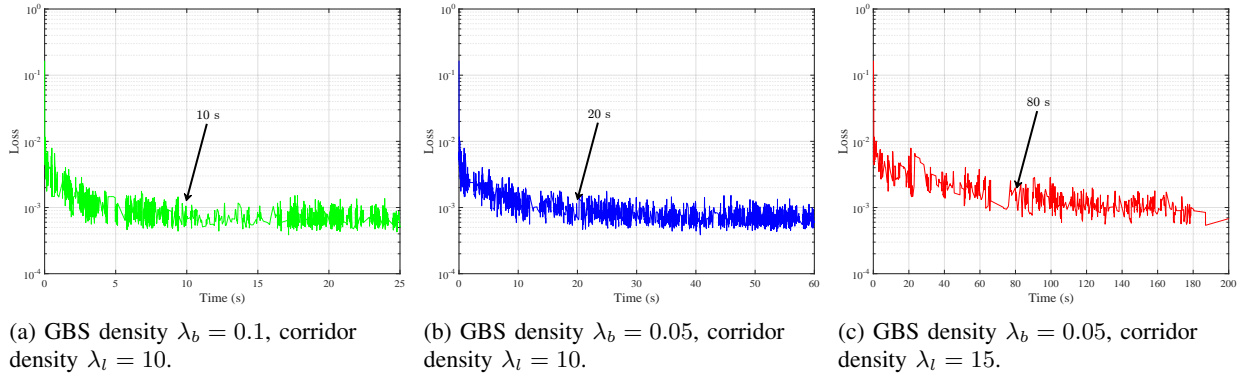


Fig. 10. Convergence of the proposed AFL under different UAM system settings. These results show that, a high density of GBSs will speed up the convergence, while dense UAM corridors lead to a low convergence rate.

convergence of the FNN-based turbulence prediction model. However, in our proposed AFL framework, we introduce the monotonically decreasing function $g_1(\cdot)$ to mitigate the impact of the outdated local parameters on the global aggregation and facilitate the overall convergence.

Fig. 10 shows the convergence of the proposed AFL framework under different UAM parameter settings. As shown in Fig. 10 (a) and (b), when the density of GBS λ_b increases, the convergence rate of the AFL framework also speeds up (i.e., the convergence time switches from 20 s to 10 s). The reason is that, a large density λ_b of GBSs can lead to a better SIR at the receiving GBSs and more frequent uplink-downlink learning model transmission between GBS and UAM aircraft. Hence, for a given time period, the total number of communication rounds will increase and the convergence rate will increase. Also, with a better SIR, the trained FNN parameters can be quickly transmitted to the GBSs, reducing staleness and improving the convergence. Moreover, from Fig. 10 (b) and (c), we can observe that as the density of corridors λ_l increases, the convergence rate becomes slower (i.e., the convergence time switches from 20 s to 80 s). This is due to the fact that more corridors will lead to more interfering aircraft in the wireless network and the air-to-ground communication link will experience a low SIR. Hence, the frequency of FNN parameters transmission between the GBS and UAM aircraft will be low and the staleness of local FNN parameters will also increase, reducing the convergence rate.

VI. CONCLUSIONS

In this paper, we have characterized the connectivity performance of the aircraft-to-GBS communication network in UAM. In particular, we have used PCP and PLP to capture the relative

location of corridors around their CPs where their relative distance between them is modeled by two distributions: truncated Gaussian distribution and uniform distribution. Next, we have characterized the distribution of aircraft on each corridor and GBSs by using, respectively, one-dimensional and two-dimensional PPP. Using this system setup, we have derived new theoretical results for the SIR-based connectivity probability when the aircraft communicates to its closest GBS and the staleness distribution associated to local FNN parameters. Based on the wireless connectivity study, we have proposed a wireless-enabled AFL framework to collaboratively learn the FNN-based turbulence prediction model among UAM aircraft. In particular, a staleness-aware AFL has been introduced to mitigate the impact of staleness associated to local FNN parameters on the overall convergence. We have also performed a rigorous convergence study to determine the convergence rate and showcase the merits of considering staleness in the AFL framework design. Simulation results corroborate our connectivity analysis for UAM and show how different system settings affect the overall connectivity performance. Moreover, the results show that the proposed AFL framework outperforms the conventional synchronous FL counterparts and AFL framework without considering the staleness. In addition, the results highlight the necessity of optimizing the UAM parameter setting and wireless network design to improve the turbulence prediction model convergence and UAM aircraft wireless connectivity.

APPENDIX

A. Proof of Lemma 2

The Laplace transform of interference at the typical GBS can be derived as follows

$$\begin{aligned}
\mathcal{L}(s) &= \mathbb{E} \left[\exp \left(-s \sum_{i \in \Phi} \sum_{j \in \Psi_i} \sum_{k \in \Omega_{i,j}} g'(f^2(x_1, x_2, u, r, \theta) + h^2)^{-\frac{\alpha}{2}} \right) \right] \\
&= \mathbb{E} \left[\prod_{i \in \Phi} \prod_{j \in \Psi_i} \prod_{k \in \Omega_{i,j}} \mathbb{E}_{g'} \exp \left(-s g'(f^2(x_1, x_2, u, r, \theta) + h^2)^{-\frac{\alpha}{2}} \right) \right] \\
&\stackrel{(a)}{=} \mathbb{E} \left[\prod_{i \in \Phi} \prod_{j \in \Psi_i} \prod_{k \in \Omega_{i,j}} \left(1 + \frac{s(f^2(x_1, x_2, u, r, \theta) + h^2)^{-\frac{\alpha}{2}}}{m} \right)^{-m} \right] \\
&= \mathbb{E} \left[\prod_{i \in \Phi} \prod_{j \in \Psi_i} \mathbb{E}_{\Omega_{i,j}} \prod_{k \in \Omega_{i,j}} \left(1 + \frac{s(f^2(x_1, x_2, u, r, \theta) + h^2)^{-\frac{\alpha}{2}}}{m} \right)^{-m} \right]
\end{aligned}$$

$$\begin{aligned}
&\stackrel{(b)}{=} \mathbb{E} \left[\prod_{i \in \Phi} \prod_{j \in \Psi_i} e^{-\lambda_t \int_{\mathbb{R}} 1 - \left(\left(1 + \frac{s(f^2(x_1, x_2, u, r, \theta) + h^2)^{-\frac{\alpha}{2}}}{m} \right)^{-m} \right) dt} \right] \\
&= \mathbb{E} \left[\prod_{i \in \Phi} \mathbb{E}_{\Psi_i} \prod_{j \in \Psi_i} \underbrace{e^{-\lambda_t \int_{\mathbb{R}} 1 - \left(\left(1 + \frac{s(f^2(x_1, x_2, u, r, \theta) + h^2)^{-\frac{\alpha}{2}}}{m} \right)^{-m} \right) dt}}_{\mathcal{K}_1(x_1, x_2, r, \theta)} \right] \\
&\stackrel{(c)}{=} \mathbb{E}_{\Phi} \left[\prod_{i \in \Phi} \sum_{n=0}^N \underbrace{\left(\int_{\mathbb{R}^+} \int_0^{2\pi} \mathcal{K}_1(x_1, x_2, r, \theta) f_R(r) f_{\theta}(\theta) d\theta dr \right)^n}_{\mathcal{K}_2(x_1, x_2)} \mathbb{P}(n|n \leq N) \right] \\
&\stackrel{(d)}{=} \exp \left(-\lambda_c \int_{\mathbb{R}^2} \left(1 - \sum_{n=0}^N (\mathcal{K}_2(x_1, x_2))^n \mathbb{P}(n|n \leq N) \right) dx \right), \tag{17}
\end{aligned}$$

where (a) follows the Gamma distribution of Nakagami fading channel gains, (b) and (d) are based on the probability generating functional (PGFL) of a PPP [27]. In (c), we use the fact that the number of corridors is Poisson distributed conditioned on total being less than N . By converting from Cartesian to polar coordinates with $x_1 = l \cos \phi$ and $x_2 = l \sin \phi$ in (17), we can the final results in (5).

B. Proof of Theorem 1

The connectivity probability can be calculated as follows

$$\begin{aligned}
\mathbb{P}_{\text{conn}} &= \mathbb{E} \left[\mathbb{P} \left(\frac{g(h^2 + \beta^2)^{-\frac{\alpha}{2}}}{I} \geq \gamma | \beta \right) \right] = \mathbb{E} \left[\mathbb{P} \left(g \geq \frac{\gamma I}{(h^2 + \beta^2)^{-\frac{\alpha}{2}}} | \beta \right) \right] \\
&\stackrel{(a)}{\approx} 1 - \mathbb{E} \left[\left(1 - \exp \left(\frac{-\eta \gamma I}{(h^2 + \beta^2)^{-\frac{\alpha}{2}}} \right) \right)^m | \beta \right] \\
&\stackrel{(b)}{=} \sum_{\hat{m}=1}^m (-1)^{\hat{m}+1} \binom{m}{\hat{m}} \mathbb{E} \left[\exp \left(\frac{-\hat{m} \eta \gamma I}{(h^2 + \beta^2)^{-\frac{\alpha}{2}}} \right) | \beta \right] \\
&\stackrel{(c)}{=} \int_{\mathbb{R}^+} \sum_{\hat{m}=1}^m (-1)^{\hat{m}+1} \binom{m}{\hat{m}} \mathcal{L}(\hat{m} \eta \gamma (h^2 + \beta^2)^{\frac{\alpha}{2}}) f_B(\beta) d\beta, \tag{18}
\end{aligned}$$

where (a) is based on the approximated tail probability of a Gamma function [35], (b) follows the Binomial theorem and the assumption that m is an integer, and (c) follows the definition of Laplace transform of interference and the fact that the distance between the aircraft and GBS is a random variable.

C. Proof of Lemma 3

Consider the CP for the arbitrarily selected corridor is (x_1, x_2) and the relative location of corridor to the CP is determined by the distance r and the angle $\theta \in [0, 2\pi)$ between the positive x -axis and the line passing through the CP and being perpendicular to the corridor. In this case, we can derive that any point (y_1, y_2) on the corridor will meet the following equality constraint:

$$y_2 - \tan \hat{\theta} y_1 - (x_2 + r \sin \theta) + \tan \hat{\theta} (x_1 + r \cos \theta) = 0, \quad (19)$$

where $\hat{\theta} = \begin{cases} \theta + \frac{\pi}{2}, & \text{if } \theta \in [0, \frac{\pi}{2}), \\ \theta - \frac{\pi}{2}, & \text{if } \theta \in [\frac{\pi}{2}, \frac{3\pi}{2}), \\ \theta - \frac{3\pi}{2}, & \text{if } \theta \in [\frac{3\pi}{2}, 2\pi). \end{cases}$ The distance between the corridor and the center of the circular area can be calculated as [36]

$$d = \frac{|\tan \hat{\theta} (x_1 + r \cos \theta) - (x_2 + r \sin \theta)|}{\sqrt{1 + (\tan^2 \hat{\theta})}} = |\cos \hat{\theta}| |\tan \hat{\theta} (x_1 + r \cos \theta) - (x_2 + r \sin \theta)|. \quad (20)$$

Hence, the length of corridor can be expressed as

$$L = 2\sqrt{R^2 - d^2} = 2\sqrt{R^2 - \mathcal{T}_1}, \quad (21)$$

where

$$\begin{aligned} \mathcal{T}_1 &= \sin^2 \hat{\theta} (x_1^2 + 2x_1 r \cos \theta + r^2 \cos^2 \theta) - 2 \sin \hat{\theta} \cos \hat{\theta} (x_1 x_2 + x_1 r \sin \theta + x_1 r \sin \theta + x_2 r \cos \theta \\ &\quad + r^2 \sin \theta \cos \theta) + \cos^2 \hat{\theta} (x_2^2 + 2x_2 r \cos \theta + r^2 \cos^2 \theta) \\ &\stackrel{(a)}{=} \cos^2 \theta (x_1^2 + 2x_1 r \cos \theta + r^2 \cos^2 \theta) - 2 \sin \theta \cos \theta (x_1 x_2 + x_1 r \sin \theta + x_1 r \sin \theta + x_2 r \cos \theta \\ &\quad + r^2 \sin \theta \cos \theta) + \sin^2 \theta (x_2^2 + 2x_2 r \cos \theta + r^2 \cos^2 \theta) \\ &\stackrel{(b)}{=} x_1^2 \cos^2 \theta + 2x_1 r \cos^3 \theta + r^2 \cos^4 \theta + 2x_1 x_2 \sin \theta \cos \theta + 2x_1 r \sin^2 \theta \cos \theta + 2x_2 r \sin \theta \cos^2 \theta \\ &\quad + 2r^2 \sin^2 \theta \cos^2 \theta + \sin^2 \theta x_2^2 + 2x_2 r \sin^3 \theta + r^2 \sin^4 \theta \\ &= x_1^2 \cos^2 \theta + 2x_1 r \cos \theta + r^2 + 2x_1 x_2 \sin \theta \cos \theta + x_2^2 \sin^2 \theta + 2x_2 r \sin \theta \\ &= (x_1 \cos \theta + x_2 \sin \theta + r)^2, \end{aligned} \quad (22)$$

where in (a), we use the relationship between θ and $\hat{\theta}$, and in (b), we simplify the results by using the basic trigonometry properties, e.g., $\cos^2 \theta + \sin^2 \theta = 1$. After substituting (22) into (21), the length of the corridor intercepting the circular area with radius R can be calculated. Based on the distribution of r and θ , we can obtain the expected length as shown in (9).

D. Proof of Theorem 2

The expected number of aircraft associated to each GBS is

$$\begin{aligned}
W &= \mathbb{E} \left(\frac{W_1 \sum_{i \in \Phi} \lambda_t L}{W_2} \right) = \mathbb{E} \left(\frac{W_1 \sum_{i \in \Phi} \lambda_t \mathbb{E}(L)}{W_2} \right) \\
&= \mathbb{E} \left(\frac{W_1 \sum_{n=0}^N \lambda_t \mathbb{E}(L) n \mathbb{P}(n|n < N)}{W_2} \right) \\
&= \left(\frac{\mathbb{E}(W_1) \sum_{n=0}^N \lambda_t \mathbb{E}(L) n \mathbb{P}(n|n < N)}{\mathbb{E}(W_2)} \right) \\
&\stackrel{(a)}{=} \left(\frac{\lambda_c \pi R^2 \sum_{n=0}^N \lambda_t \mathbb{E}(L) n \mathbb{P}(n|n < N)}{\lambda_b \pi R^2} \right), \tag{23}
\end{aligned}$$

where W_1 and W_2 , respectively, represent the total number of CPs and GBSs. In (a), we use the basic Poisson distribution property and the fact that the density of two-dimensional PPP distributed of CPs and GBSs will be the unit density times the area of the circular space.

E. Proof of Theorem 3

To prove Theorem 3, we first obtain the upper bound of $f(\mathbf{w})$:

$$\begin{aligned}
f(\mathbf{w}_{i+1}) &\stackrel{(a)}{\leq} f(\mathbf{w}_i) + \langle \nabla f(\mathbf{w}_i), \mathbf{w}_{i+1} - \mathbf{w}_i \rangle + \frac{1}{2!} (\mathbf{w}_{i+1} - \mathbf{w}_i)^T \nabla^2 f(\mathbf{w}_i) (\mathbf{w}_{i+1} - \mathbf{w}_i) \\
&\stackrel{(b)}{\leq} f(\mathbf{w}_i) + \langle \nabla f(\mathbf{w}_i), \mathbf{w}_{i+1} - \mathbf{w}_i \rangle + \frac{L}{2} \|\mathbf{w}_{i+1} - \mathbf{w}_i\|^2 \\
&\stackrel{(c)}{\leq} f(\mathbf{w}_i) + \langle \nabla f(\mathbf{w}_i), -\eta_i g_1(\delta_{k,i}) \frac{s_k}{s_K} \nabla f_k(\mathbf{w}_{\delta_{k,i}}) \rangle + \frac{L}{2} \eta_i^2 g_1^2(\delta_{k,i}) \left(\frac{s_k}{s_K} \right)^2 \|\nabla f_k(\mathbf{w}_{\delta_{k,i}})\|^2, \tag{24}
\end{aligned}$$

where (a) follows the Taylor expansion, (b) is based on the assumption of the Lipschitz continuity, and the inequality is derived due to the basic relationship between \mathbf{w}_{i+1} and \mathbf{w}_i .

In the results (24), we need to consider two types of randomness, i.e., the aircraft $k \in \mathcal{K}$ participated into the learning model parameters update and the staleness value $\delta_{k,i}$. First, we take expectation for both side of (24) in terms of the participating aircraft as follows

$$\begin{aligned}
\mathbb{E}_k(f(\mathbf{w}_{i+1})) &\leq f(\mathbf{w}_i) - \eta_i g_1(\delta_{k,i}) \frac{1}{K} \langle \nabla f(\mathbf{w}_i), \mathbb{E}(\nabla f_k(\mathbf{w}_{\delta_{k,i}})) \rangle + \frac{L}{2} \eta_i^2 g_1^2(\delta_{k,i}) \frac{1}{K^2} \|\nabla f_k(\mathbf{w}_{\delta_{k,i}})\|^2 \\
&\stackrel{(a)}{\leq} f(\mathbf{w}_i) - \eta_i g_1(\delta_{k,i}) \frac{1}{K} \langle \nabla f(\mathbf{w}_i), \nabla f(\mathbf{w}_{\delta_{k,i}}) \rangle + \frac{L}{2} \eta_i^2 g_1^2(\delta_{k,i}) \frac{1}{K^2} \|\nabla f_k(\mathbf{w}_{\delta_{k,i}})\|^2 \\
&\stackrel{(b)}{\leq} f(\mathbf{w}_i) - \eta_i g_1(\delta_{k,i}) \frac{1}{2K} \left(\|\nabla f(\mathbf{w}_i)\|^2 + \|\nabla f(\mathbf{w}_{\delta_{k,i}})\|^2 - \|\nabla f(\mathbf{w}_i) - \nabla f(\mathbf{w}_{\delta_{k,i}})\|^2 \right) \\
&\quad + \frac{L}{2} \eta_i^2 g_1^2(\delta_{k,i}) \frac{1}{K^2} \|\nabla f_k(\mathbf{w}_{\delta_{k,i}})\|^2
\end{aligned}$$

$$\begin{aligned}
&= f(\mathbf{w}_i) - \frac{\eta_i g_1(\delta_{k,i})}{2K} \left(\|\nabla f(\mathbf{w}_i)\|^2 + \|\nabla f(\mathbf{w}_{\delta_{k,i}})\|^2 \right) \\
&\quad + \frac{\eta_i g_1(\delta_{k,i})}{2K} \left(\|\nabla f(\mathbf{w}_i) - \nabla f(\mathbf{w}_{\delta_{k,i}})\|^2 \right) + \frac{L\eta_i^2 g_1^2(\delta_{k,i})}{2K^2} \|\nabla f_k(\mathbf{w}_{\delta_{k,i}})\|^2 \\
&\stackrel{(c)}{\leq} f(\mathbf{w}_i) - \frac{\eta_i g_1(\delta_{k,i})}{2K} \left(\|\nabla f(\mathbf{w}_i)\|^2 + \|\nabla f(\mathbf{w}_{\delta_{k,i}})\|^2 \right) \\
&\quad + \frac{L\eta_i^2 g_1^2(\delta_{k,i})}{2K^2} g_2(\delta_{k,i}) \mathbb{E}[\|\nabla f(\mathbf{w}_{\delta_{k,i}})\|^2] + \underbrace{\frac{L\eta_i^2 g_1^2(\delta_{k,i})}{2K^2} \|\nabla f_k(\mathbf{w}_{\delta_{k,i}})\|^2}_{\mathcal{T}_2}, \tag{25}
\end{aligned}$$

where in (a) follows the fact that, for aircraft $k \in \mathcal{K}$, the gradient of its local training data is the unbiased estimation to the gradient representation for the data across all aircraft, i.e., $\mathbb{E}(f_k(\mathbf{w})) = \mathbb{E}(f(\mathbf{w}))$, $\forall k \in \mathcal{K}$ [37]. The changes in (b) are based on $\langle \mathbf{w}, \hat{\mathbf{w}}_1 \rangle = \frac{1}{2}(\|\mathbf{w}\|^2 + \|\hat{\mathbf{w}}_1\|^2 - \|\mathbf{w} - \hat{\mathbf{w}}_1\|^2)$. In (c), we use the third assumption regarding the variance between the global gradient descent at an arbitrarily communication round i and the outdated local gradient at a random aircraft. In particular, \mathcal{T}_2 can be further simplified as

$$\begin{aligned}
\mathcal{T}_2 &= \mathbb{E}_k(\|\nabla f_k(\mathbf{w}_{\delta_{k,i}}) - f(\mathbf{w}_{\delta_{k,i}}) + f(\mathbf{w}_{\delta_{k,i}})\|^2) \\
&= \mathbb{E}_k(\|\nabla f_k(\mathbf{w}_{\delta_{k,i}}) - f(\mathbf{w}_{\delta_{k,i}})\|^2) + \mathbb{E}_k(\|f(\mathbf{w}_{\delta_{k,i}})\|^2) + 2\mathbb{E}_k\langle \nabla f_k(\mathbf{w}_{\delta_{k,i}}) - f(\mathbf{w}_{\delta_{k,i}}), f(\mathbf{w}_{\delta_{k,i}}) \rangle \\
&= \mathbb{E}_k(\|\nabla f_k(\mathbf{w}_{\delta_{k,i}}) - f(\mathbf{w}_{\delta_{k,i}})\|^2) + \mathbb{E}_k(\|f(\mathbf{w}_{\delta_{k,i}})\|^2) \\
&\stackrel{(a)}{\leq} \phi^2 + \mathbb{E}(\|f(\mathbf{w}_{\delta_{k,i}})\|^2), \tag{26}
\end{aligned}$$

where in (a), we use the second assumption. After replacing \mathcal{T}_2 with the results obtained in (26), we can further simplify (25) as

$$\begin{aligned}
\mathbb{E}_k(f(\mathbf{w}_{i+1})) &\leq f(\mathbf{w}_i) - \frac{\eta_i g_1(\delta_{k,i})}{2K} \left(\|\nabla f(\mathbf{w}_i)\|^2 + \|\nabla f(\mathbf{w}_{\delta_{k,i}})\|^2 \right) \\
&\quad + \frac{L\eta_i^2 g_1(\delta_{k,i})}{2K^2} g_2(\delta_{k,i}) \mathbb{E}[\|\nabla f(\mathbf{w}_{\delta_{k,i}})\|^2] + \frac{L\eta_i^2 g_1^2(\delta_{k,i})}{2K^2} \left(\phi^2 + \mathbb{E}(\|f(\mathbf{w}_{\delta_{k,i}})\|^2) \right) \\
&= f(\mathbf{w}_i) - \frac{\eta_i g_1(\delta_{k,i})}{2K} \left(\|\nabla f(\mathbf{w}_i)\|^2 \right) + \frac{L\eta_i^2 g_1^2(\delta_{k,i}) \phi^2}{2K^2} \\
&\quad + \left(\frac{L\eta_i^2 g_1(\delta_{k,i})}{2K^2} g_2(\delta_{k,i}) + \frac{L\eta_i^2 g_1^2(\delta_{k,i})}{2K^2} - \frac{\eta_i g_1(\delta_{k,i})}{2K} \right) \mathbb{E}[\|\nabla f(\mathbf{w}_{\delta_{k,i}})\|^2]. \tag{27}
\end{aligned}$$

Taking expectation of (27) in terms of the staleness, we have

$$\begin{aligned}
\mathbb{E}_{k,\delta}(f(\mathbf{w}_{i+1})) &\leq f(\mathbf{w}_i) - \frac{\eta_i \mathbb{E}_\delta(g_1(\delta_{k,i}))}{2K} \left(\|\nabla f(\mathbf{w}_i)\|^2 \right) + \frac{L\eta_i^2 \mathbb{E}_\delta(g_1^2(\delta_{k,i})) \phi^2}{2K^2} \\
&\quad + \mathbb{E}_\delta \left(\left(\frac{L\eta_i^2 g_1(\delta_{k,i})}{2K^2} g_2(\delta_{k,i}) + \frac{L\eta_i^2 g_1^2(\delta_{k,i})}{2K^2} - \frac{\eta_i g_1(\delta_{k,i})}{2K} \right) \mathbb{E}[\|\nabla f(\mathbf{w}_{\delta_{k,i}})\|^2] \right).
\end{aligned}$$

If $L\eta_i g_2(\delta_{k,i}) + L\eta_i g_1(\delta_{k,i}) - K \leq 0$, $\forall \delta_{k,i} \in \mathbb{R}_+$, we can obtain the convergence rate as presented

in Theorem 3.

F. Proof of Corollary 3

After subtracting $f(\mathbf{w}^*)$ in both sides of (12), we have

$$\begin{aligned}
\mathbb{E}(f(\mathbf{w}_{i+1})) - f(\mathbf{w}^*) &\leq f(\mathbf{w}_i) - f(\mathbf{w}^*) - \frac{\eta_i \mathbb{E}_\delta(g_1(\delta))}{2K} \|\nabla f(\mathbf{w}_i)\|^2 + \frac{L\eta_i^2 (\mathbb{V}_\delta(g_1(\delta)) + \mathbb{E}_\delta^2(g_1(\delta))) \phi^2}{2K^2} \\
&\stackrel{(a)}{\leq} f(\mathbf{w}_i) - f(\mathbf{w}^*) - \frac{\eta_i \mathbb{E}_\delta(g_1(\delta))c}{K} (f(\mathbf{w}_i) - f(\mathbf{w}^*)) + \frac{L\eta_i^2 (\mathbb{V}_\delta(g_1(\delta)) + \mathbb{E}_\delta^2(g_1(\delta))) \phi^2}{2K^2} \\
&= \left(1 - \frac{\eta_i \mathbb{E}_\delta(g_1(\delta))c}{K}\right) (f(\mathbf{w}_i) - f(\mathbf{w}^*)) + \frac{L\eta_i^2 (\mathbb{V}_\delta(g_1(\delta)) + \mathbb{E}_\delta^2(g_1(\delta))) \phi^2}{2K^2} \\
&= \left(1 - \frac{\eta_i \mathbb{E}_\delta(g_1(\delta))c}{K}\right)^2 (f(\mathbf{w}_{i-1}) - f(\mathbf{w}^*)) + \frac{L\eta_i^2 (\mathbb{V}_\delta(g_1(\delta)) + \mathbb{E}_\delta^2(g_1(\delta))) \phi^2}{2K^2} \\
&+ \left(1 - \frac{\eta_i \mathbb{E}_\delta(g_1(\delta))c}{K}\right) \left(\frac{L\eta_i^2 (\mathbb{V}_\delta(g_1(\delta)) + \mathbb{E}_\delta^2(g_1(\delta))) \phi^2}{2K^2}\right) \\
&\dots \\
&= \left(1 - \frac{\eta_i \mathbb{E}_\delta(g_1(\delta))c}{K}\right)^{i+1} (f(\mathbf{w}_0) - f(\mathbf{w}^*)) \\
&+ \sum_{j=0}^i \left(1 - \frac{\eta_i \mathbb{E}_\delta(g_1(\delta))c}{K}\right)^j \frac{L\eta_i^2 (\mathbb{V}_\delta(g_1(\delta)) + \mathbb{E}_\delta^2(g_1(\delta))) \phi^2}{2K^2}, \tag{28}
\end{aligned}$$

where in (a), we use the lower bound for the norm $f(\mathbf{w})$, i.e., $\|\nabla f(\mathbf{w}_i)\|^2 \geq 2c(f(\mathbf{w}_i) - f(\mathbf{w}^*))$ [38]. Based on the basic property of geometric progression, we can have the simplified results in Corollary 3.

REFERENCES

- [1] T. Zeng, O. Semiari, W. Saad, and M. Bennis, "Performance analysis of aircraft to ground communication networks in urban air mobility (UAM)," in *Proc. of IEEE Global Communications Conference (GLOBECOM)*, Madrid, Spain, Dec. 2021.
- [2] United Nations, Department of Economic and Social Affairs, "World urbanization prospects the 2018 revision," 2018.
- [3] Federal Aviation Administration, "Concept of operations v1.0, foundational principles, roles and responsibilities, scenarios and operational threads, urban air mobility (UAM)," Jun. 2020.
- [4] Booz Allen Hamilton, "Urban air mobility (UAM) market study," 2018.
- [5] C. Al Haddad, E. Chaniotakis, A. Straubinger, K. Plötner, and C. Antoniou, "Factors affecting the adoption and use of urban air mobility," *Transportation research part A: policy and practice*, vol. 132, pp. 696–712, Feb. 2020.
- [6] P. D. Vascik, J. Cho, V. Bulusu, and V. Polishchuk, "Geometric approach towards airspace assessment for emerging operations," *Journal of Air Transportation*, vol. 28, no. 3, pp. 124–133, May 2020.
- [7] A. Rodionova, Y. V. Pant, K. Jang, H. Abbas, and R. Mangharam, "Learning-to-fly: Learning-based collision avoidance for scalable urban air mobility," in *Proc. of IEEE International Conference on Intelligent Transportation Systems (ITSC)*, Rhodes, Greece, Sept. 2020.
- [8] P. Pradeep and P. Wei, "Energy-efficient arrival with RTA constraint for multirotor eVTOL in urban air mobility," *Journal of Aerospace Information Systems*, vol. 16, no. 7, pp. 263–277, Jul. 2019.
- [9] W. B. Cotton and D. J. Wing, "Airborne trajectory management for urban air mobility," in *Proc. of Aviation Technology, Integration, and Operations Conference*, Atlanta, GA, USA, Jun. 2018.

- [10] X. Yang, L. Deng, and P. Wei, "Multi-agent autonomous on-demand free flight operations in urban air mobility," in *Proc. of AIAA Aviation 2019 Forum*, Dallas, TX, USA, Jun. 2019.
- [11] T. Donato and A. Ficarella, "A modeling approach for the effect of battery aging on the performance of a hybrid electric rotorcraft for urban air-mobility," *Aerospace*, vol. 7, no. 5, pp. 56–75, May 2020.
- [12] J. D. Anderson Jr, *Fundamentals of aerodynamics*. Tata McGraw-Hill Education, 2010.
- [13] R. Wang, K. Kashinath, M. Mustafa, A. Albert, and R. Yu, "Towards physics-informed deep learning for turbulent flow prediction," in *Proc. of ACM SIGKDD International Conference on Knowledge Discovery and Data Mining*, New York, NY, USA, Jul. 2020.
- [14] D. Kochkov, J. A. Smith, A. Alieva, Q. Wang, M. P. Brenner, and S. Hoyer, "Machine learning accelerated computational fluid dynamics," *arXiv preprint arXiv:2102.01010*, 2021.
- [15] Z. Li, N. Kovachki, K. Azizzadenesheli, B. Liu, K. Bhattacharya, A. Stuart, and A. Anandkumar, "Fourier neural operator for parametric partial differential equations," *arXiv preprint arXiv:2010.08895*, 2020.
- [16] M. Chen, H. V. Poor, W. Saad, and S. Cui, "Wireless communications for collaborative federated learning," *IEEE Communications Magazine, Special Issue on Communication Technologies for Efficient Edge Learning*, vol. 58, no. 12, pp. 48–54, Dec. 2020.
- [17] J. Konečný, H. B. McMahan, D. Ramage, and P. Richtárik, "Federated optimization: Distributed machine learning for on-device intelligence," *arXiv preprint arXiv:1610.02527*, 2016.
- [18] T. Li, A. Sahu, M. Zaheer, M. Sanjabi, A. Talwalkar, and V. Smith, "Federated optimization in heterogeneous networks," in *Proc. of ACM Conference on Machine Learning and Systems*, Austin, TX, USA, Mar. 2020.
- [19] K. Bonawitz, H. Eichner, W. Grieskamp, D. Huba, A. Ingerman, V. Ivanov, C. Kiddon, J. Konečný, S. Mazzocchi, H. B. McMahan *et al.*, "Towards federated learning at scale: System design," *arXiv preprint arXiv:1902.01046*, 2019.
- [20] A. Reiszadeh, A. Mokhtari, H. Hassani, A. Jadbabaie, and R. Pedarsani, "Fedpaq: A communication-efficient federated learning method with periodic averaging and quantization," in *Proceedings of International Conference on Artificial Intelligence and Statistics*, Palermo, Italy, Aug. 2020.
- [21] T. Zeng, O. Semiari, M. Chen, W. Saad, and M. Bennis, "Federated learning on the road: Autonomous controller design for connected and autonomous vehicles," *arXiv preprint arXiv:2102.03401*, 2021.
- [22] Y. Chen, X. Sun, and Y. Jin, "Communication-efficient federated deep learning with layerwise asynchronous model update and temporally weighted aggregation," *IEEE Transactions on Neural Networks and Learning Systems*, vol. 31, no. 10, pp. 4229–4238, Oct. 2020.
- [23] Y. Lu, X. Huang, Y. Dai, S. Maharjan, and Y. Zhang, "Differentially private asynchronous federated learning for mobile edge computing in urban informatics," *IEEE Transactions on Industrial Informatics*, vol. 16, no. 3, pp. 2134–2143, Mar. 2020.
- [24] C. Xie, S. Koyejo, and I. Gupta, "Asynchronous federated optimization," *arXiv preprint arXiv:1903.03934*, 2019.
- [25] J. Nguyen, K. Malik, H. Zhan, A. Yousefpour, M. Rabbat, M. M. Esmaili, and D. Huba, "Federated learning with buffered asynchronous aggregation," *arXiv preprint arXiv:2106.06639*, 2021.
- [26] W. Dai, Y. Zhou, N. Dong, H. Zhang, and E. P. Xing, "Toward understanding the impact of staleness in distributed machine learning," *arXiv preprint arXiv:1810.03264*, 2018.
- [27] S. N. Chiu, D. Stoyan, W. S. Kendall, and J. Mecke, *Stochastic geometry and its applications*. John Wiley & Sons, 2013.
- [28] M. Haenggi, *Stochastic geometry for wireless networks*. Cambridge University Press, 2012.
- [29] V. V. Chetlur and H. S. Dhillon, "Coverage analysis of a vehicular network modeled as cox process driven by poisson line process," *IEEE Transactions on Wireless Communications*, vol. 17, no. 7, pp. 4401–4416, Jul. 2018.
- [30] C. Choi and F. Baccelli, "Poisson cox point processes for vehicular networks," *IEEE Transactions on Vehicular Technology*, vol. 67, no. 10, pp. 10 160–10 165, Oct. 2018.
- [31] J. G. Andrews, A. K. Gupta, and H. S. Dhillon, "A primer on cellular network analysis using stochastic geometry," *arXiv preprint arXiv:1604.03183*, 2016.
- [32] L. Bottou, F. Curtis, and J. Nocedal, "Optimization methods for large-scale machine learning," *SIAM Review*, vol. 60, no. 2, pp. 223–311, May 2018.
- [33] A. A. Boritchev, "Turbulence for the generalised burgers equation," *Russian Mathematical Surveys*, vol. 69, no. 6, pp. 957–994, Dec. 2014.
- [34] S. A. Miller, *Toward a nonlinear acoustic analogy: turbulence as a source of sound and nonlinear propagation*. National Aeronautics and Space Administration, Langley Research Center, 2015.
- [35] T. Bai and R. W. Heath, "Coverage and rate analysis for millimeter-wave cellular networks," *IEEE Transactions on Wireless Communications*, vol. 14, no. 2, pp. 1100–1114, Feb. 2015.
- [36] B. Spain, *Analytical conics*. Courier Corporation, 2007.
- [37] B. Chen, Y. Xu, and A. Shrivastava, "Fast and accurate stochastic gradient estimation," in *Proc. of Advances in Neural Information Processing Systems (NeurIPS)*, Vancouver, Canada, Dec. 2019.
- [38] T. Zeng, O. Semiari, M. Mozaffari, M. Chen, W. Saad, and M. Bennis, "Federated learning in the sky: Joint power allocation and scheduling with UAV swarms," in *Proc. of IEEE International Conference on Communications (ICC)*, Dublin, Ireland, June 2020.